Biomaterials Science

ROYAL SOCIETY OF CHEMISTRY

PAPER

View Article Online
View Journal | View Issue

Cite this: *Biomater. Sci.*, 2021, **9**, 4099

Influence of high-pressure torsion deformation on the corrosion behaviour of a bioresorbable Mg-based alloy studied by positron annihilation

Philipp Brunner, *[a] Florian Brumbauer, [a] Eva-Maria Steyskal, [a] Oliver Renk, [b] Annelie-Martina Weinberg,[c] Hartmuth Schroettner[d] and Roland Würschum [e]

The effect of high-pressure torsion (HPT) on the corrosion behavior of extruded ZX00 (Mg–0.45wt%Zn–0.45wt%Ca) in phosphate buffered saline solution is investigated. MgCaZn alloys are promising candidates for the use as bioresorbable implant materials and, therefore, are in the focus of current research. To improve their strength, severe plastic deformation, *e.g. via* the technique of HPT, can be used. Positron lifetime spectroscopy (PLS) is applied as sensitive tool for studying open-volume defects which evolve during HPT processing and subsequent corrosion. The studies were complemented by electrochemical impedance spectroscopy (EIS). In the uncorroded state, grain boundaries are the major type of positron trap as quantitatively analysed by means of diffusion-reaction models for positron trapping and annihilation in fine-grained alloys. Upon corrosion, positronium formation and annihilation indicate larger open-volume structures, such as pores and cracks, in the emerging corrosion product and oxide layers. Both PLS and EIS clearly show that HPT-deformation strongly reduces the resistance against corrosion. Evidence is found for corrosion-induced open-volume defects, presumably related to hydrogen, in deeper parts of the material below the corrosion layer.

Received 29th January 2021,
Accepted 23rd April 2021

DOI: 10.1039/d1bm00166c

rsc.li/biomaterials-science

I. Introduction

Magnesium (Mg) and its alloys are promising candidates for the use as bioresorbable implant materials and therefore in the focus of current biomaterials research. For non-permanent applications, such as fracture fixation, they offer major advantages compared to the commonly used implants made of titanium or stainless steel. Mg-based implant materials support fracture healing by continuously transferring load back to the bone as they are resorbed. Additionally, they do not need to be explanted after the healing process has finished.[1–3] Further advantages are their bio-compatibility, nontoxicity, low specific density and an elastic modulus close to that of human bone.[4,5] The Mg^{2+} release during the dissolution supports osteogenesis and therefore promotes the formation of healthy bone near the implant tissue interface.[6] Nevertheless, pure Mg suffers from a low strength for load-bearing implants and dissolves quickly in physiological environments, accompanied by a rapid evolution of hydrogen. The produced hydrogen causes troubles like a delayed healing process, necrosis of the surrounding tissue or can lead to encapsulated gas cavities.[2,4,7] Using suitable Mg alloys allows to both increase the materials strength and slow down the degradation rate and therefore improves the performance as implant material.[2]

Here we investigate the alloy Mg–0.45wt%Zn–0.45wt%Ca (ZX00), which only contains elements, naturally present in the human body. This material has been shown to be biocompatible with adequate degradation rates, along with a yield strength of 285 MPa.[1,7] One technique, suitable to further improve the strength of Mg alloys, is grain refinement[8] *via* severe plastic deformation, such as high-pressure torsion (HPT).[9] The effects of grain refinement on the corrosion behavior are under debate.[10–16] Corrosion preferentially takes place along crystalline defects, such as dislocations and grain boundaries, but also along second phase particles. Some authors found that the higher grain boundary density and the fragmentation of potentially present second phase particles after severe plastic deformation provide more homogeneously distributed sites for corrosion attack. Therefore a change from a localized towards a more uniform degradation process is

[a]*Institute of Materials Physics, Graz University of Technology, Petersgasse 16, 8010 Graz, Austria. E-mail: philipp.brunner@tugraz.at*
[b]*Erich Schmid Institute of Materials Science, Austrian Academy of Sciences, 8700 Leoben, Austria*
[c]*Department of Orthopaedics and Trauma, Medical University of Graz, Auenbruggerplatz 5, 8036 Graz, Austria*
[d]*Institute of Electron Microscopy and Nanoanalytics, Graz University of Technology, Steyrergasse 17, 8010 Graz, Austria*
[e]*Institute of Materials Physics, Graz University of Technology, Petersgasse 16, 8010 Graz, Austria. E-mail: wuerschum@tugraz.at*

observed. This leads to a compact corrosion product layer, which protects the underlying matrix from the corrosive environment and slows down the degradation process.[15,16] On the contrary, other authors claim that the formed corrosion product layer after severe plastic deformation has no improved passivation ability and delivers therefore no protection against the corrosive environment. The additionally introduced crystalline defects then cause an enhanced corrosion rate.[10]

In the present study, positron lifetime spectroscopy (PLS) is applied for studying open-volume defects which evolve during HPT processing and subsequent corrosion. A comparison of the positron lifetime measurements performed on ZX00 with and without HPT-deformation in dependence of corrosion time in phosphate buffered saline solution aims to assess the influence of HPT-deformation on the corrosion-induced open-volume defects. The high sensitivity of about 1 to 100 atomic ppm towards defects in the sub-nanometer range make PLS to a powerful tool for detecting vacancies, dislocations or microvoids and pores in all kinds of solids, especially in metals and semiconductors.[17–19] Since PLS with conventional positron sources probes the materials bulk, potentially arising corrosion induced open-volume defects deeper inside the sample can be investigated. As an example, evidence for crack formation inside the material in the context with hydrogen embrittlement during corrosion comes so far from, *e.g.*, electron microscopy or stress corrosion cracking tests.[20,21] Due to its sensitivity to defects in the sub-nanometer range, PLS has the capability of providing insights to very early states of this crack formation.

Positron annihilation studies of corrosion-related phenomena have been performed so far primarily by means of monoenergetic beams (see, *e.g.* ref. 22–24), to a lesser extent only by means of PALS using conventional positron sources (see, *e.g.*, ref. 22 and 25–28). The present e^+ annihilation studies are the first on the corrosion behavior of an HPT-deformed alloy and also the first on this type of Mg alloy (ZX00). The studies are complemented by electrochemical impedance spectroscopy (EIS), a well-established technique for studying corrosion phenomena.[29]

II. Experimental

The used alloy Mg–0.45wt%Zn–0.45wt%Ca (ZX00) is the same that has been studied recently by one of the coauthors.[1,7] After solution and ageing-treatments, the alloy was indirectly extruded at 325 °C. From this material, denoted $ZX00_{EXT}$ henceforth, disks with a diameter of 15 mm and a thickness of about 1 mm were cut, serving as reference samples as well as raw material for subsequent high-pressure torsion. For HPT a total of 10 revolutions with a nominal pressure of approximately 2.6 GPa was applied at room temperature, denoted $ZX00_{HPT}$ henceforth. The $ZX00_{EXT}$ and $ZX00_{HPT}$ discs were cut in 4 pieces and kept in a vacuum-desiccator with silica gel as desiccant.

The microstructure of the uncorroded material was characterized by scanning electron microscopy (SEM) along with EDX-analysis using a ZEISS Ultra 55 FESEM with an EDAX Super Octance detector. The used setup was described in detail previously.[30,31] Micrographs were recorded in channeling contrast mode. For the SEM-studies, the samples were mechanically precut and then finally prepared by ion beam technique.

The e^+ lifetime measurements were performed with a conventional positron lifetime spectrometer (in so-called fast-fast set-up) with a time resolution of 160 ps, a description of which can be found elsewhere.[32] A ^{22}Na radioactive isotope encapsulated between 5 μm thick Al foils was used as a e^+ source. The recorded spectra contained at least more than 10^6 counts and were analyzed by means of the program PALSFIT[33] after source correction. An annealed ultra high purity (XHP) Mg sample pair was used to determine the source contribution consisting of two components of 408 ps and 1500 ps with relative intensities of 16% and 3%, respectively. The $ZX00_{EXT,HPT}$-sample platelets with an initial thickness of 0.9 mm were stepwise corroded between 12 s and 48 h by immersing in phosphate buffered saline (PBS) solution, the corrosive medium used in this study. After removing the samples from the corrosive environment, they were carefully rinsed with distilled water, so that the overall well adherent corrosion product remained on the sample surface. After drying the samples in a desiccator, they were weighted with a Sartorius™ Cubis™ microbalance using a 6.6S weighting module. The PBS was prepared *via* dissolving a phosphate buffered saline tablet (ROTI FAIR PBS 7.4) in 200 ml highly pure water (ROTIPURAN p.a., ACS).

The onset of corrosion at the alloy surface was also characterized by electrochemical impedance spectroscopy (EIS). Spectra of $ZX00_{EXT,HPT}$ were recorded after 10 min of immersion, using an AUTOLAB potentiostat (AUT85934, METROHM) equipped with an EIS module (FRA32M). For this purpose, the $ZX00_{EXT,HPT}$-samples were contacted with a gold wire using commercial conduct silver. To ensure a stable contact and to avoid unintended exposure to PBS, the contact was sealed with a two-component epoxy glue. A three-electrode electrochemical cell was used for the measurements at room temperature, with the $ZX00_{EXT,HPT}$-samples serving as working electrode, a curled platinum wire as counter electrode, and an Ag/AgCl electrode in 3M-KCl as reference (RE), to which all given potentials are referred to. To reduce artifacts due to the high impedance response of the reference electrode,[34] a platinum wire in series with a 1 μF capacitance was parallel connected to RE, as recommended by the manufacturer. The EIS measurements were performed at open circuit potential (OCP) in a frequency range between 100 kHz and a few mHz with six points per decade and a 0.01 V single sine amplitude. The recorded spectra were analyzed *via* the NOVA 1.11 software.

III. Results

A. Microstructurural characterization

The base alloy material $ZX00_{EXT}$ used in the present study has recently been characterized in detail by Holweg *et al.*[1] To a

great extent (*ca.* 80%) the material exhibits a recrystallized structure with an average size of 1.7 ± 0.8 μm. The Mg matrix contains nanometric intermetallic particles composed of a Ca-rich phase, presumably of Laves-type Mg_2Ca. An average intermetallic particle size of 80 ± 35 nm was reported by Cihova *et al.*[35] for Mg–Zn–Ca alloys with a little higher concentration of Zn.

Fig. 1(a) and (b) show scanning electronmicrographs of $ZX00_{EXT}$ and $ZX00_{HPT}$, respectively, which were taken in the framework of the present study. For $ZX00_{EXT}$, structural features were found similar to that denoted above.[1] The average grain size is between 2 and 3 μm. The bright spots in the micrograph indicate the intermetallic particles (Fig. 1a), which with few exceptions are of nanometric size in the range of about 100 nm. They consist mainly of Mg (72.4 at%) and Ca (26.6 at%) and to a minor fraction of Zn according to EDX measurements (not shown), indicating the presence of a Mg_2Ca Laves phase, as expected from literature.[1] These particles are mostly formed discontinuously along grain boundaries, but some are also found within the grains. The average interparticle spacing is estimated to 1–2 μm, which is in the same range as found by Cihova *et al.*[35] for Mg–Zn–Ca alloys with a little higher concentration of Zn. After HPT processing, smaller grains, elongated along the deformation axis with an average width of 1 μm and length of 2 to 3 μm, are observed (see SEM-micrograph of $ZX00_{HPT}$, Fig. 1b). No significant change in the intermetallic particle size due to fragmentation of the precipitates is found after HPT deformation.

B. Electrochemical impedance spectroscopy

For studying the corrosion behavior, electrochemical impedance spectroscopy is applied complementary to positron annihilation. Fig. 2 shows electrochemical impedance spectra for $ZX00_{EXT}$ and $ZX00_{HPT}$ in the Nyquist plot representation recorded 10 min after immersion in PBS at their OCP values (for further details see Fig. 2). For $ZX00_{EXT}$ two capacitive loops, one in the high and the other in the medium frequency range, as well as an inductive loop for low frequencies can be discerned. After HPT processing, the measured spectrum of $ZX00_{HPT}$ changes significantly in terms of its shape and size (Fig. 2). The high frequency loop is hardly pronounced as compared to $ZX00_{EXT}$, whereas the capacitive loop in the medium

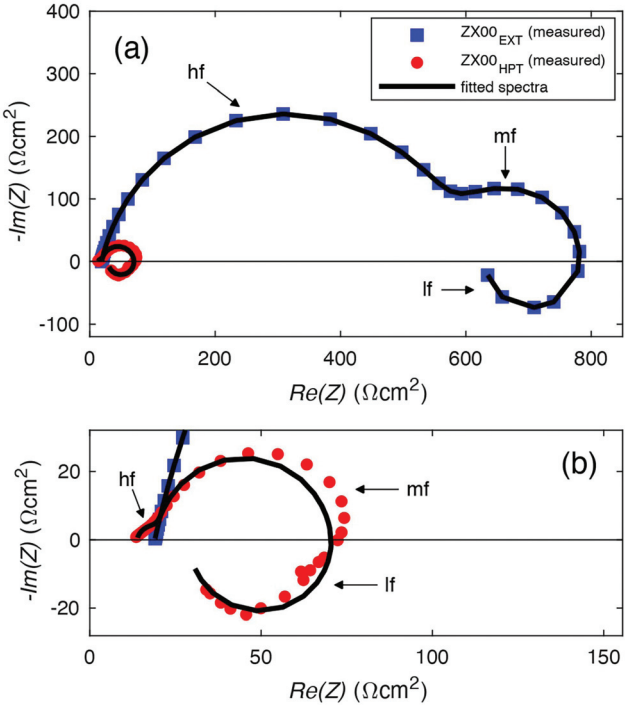

Fig. 2 (a) Impedance spectra in the Nyquist plot representation of $ZX00_{EXT}$ (blue) and of $ZX00_{HPT}$ (red) after 10 min of immersion in PBS at the OCP values of −1.705 V and −1.579 V, respectively. Frequency ranges of 100 kHz to 2.1 mHz and 100 kHz to 9.5 mHz are chosen for $ZX00_{EXT}$ and $ZX00_{HPT}$, respectively. The black lines represent the fits to the equivalent electrical circuit of Fig. 3. (b) Zoomed spectrum of $ZX00_{HPT}$. hf denotes the high frequency, mf the medium frequency, and lf the low frequency range.

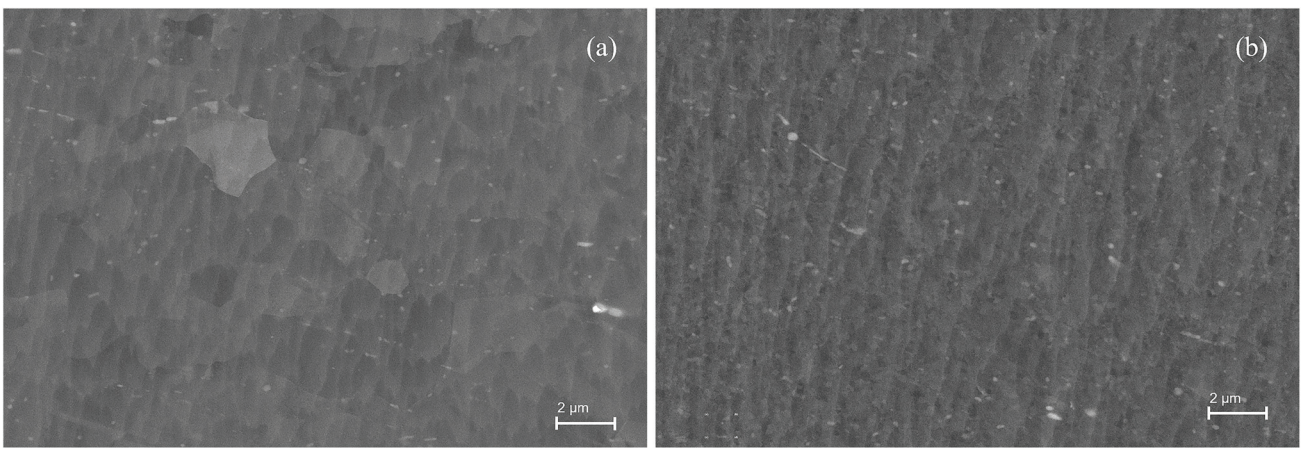

Fig. 1 SEM channeling contrast images of (a) $ZX00_{EXT}$ and (b) $ZX00_{HPT}$ microstructure. The $ZX00_{EXT}$ micrograph is recorded in extrusion direction, the $ZX00_{HPT}$ micrograph in the direction of the torsion axis.

frequency range and the inductive loop at low frequencies is clearly visible.

According to literature (*e.g.* Baril *et al.*[36] or Gomes *et al.*[37]), the high frequency capacitive loop corresponds to the charge transfer resistance parallel to the interface capacitance and the capacitive loop in the medium frequency range to the diffusion of dissolved Mg^{2+} through the porous $Mg(OH)_2$ layer. The low frequency inductive loop corresponds to the relaxation of the adsorbed intermediates Mg^{+}, which are formed during the dissolution of Mg and which cover the film free surface.

The measured spectra are analyzed by means of an equivalent electrical circuit (EEC) shown in Fig. 3, similar as used by Baril *et al.*,[36] King *et al.*,[38] or Liu *et al.*[39] The EEC takes into account the electrolyte resistance R_e and the charge transfer resistance R_{ct} associated with the cathodic hydrogen evolution at cathodic sites. The double layer capacitance at the film free areas is neglected[36] since most of the surface is covered with a thin MgO layer. The capacitance of the MgO layer is represented by the constant phase element $Y_{C_{int}}$. The resistance R_{diff} and the parallel constant phase element $Y_{C_{diff}}$ are used to describe the diffusion of Mg^{2+} through the porous corrosion layer. The inductive behavior at low frequencies is fitted by the inductance L in series with the resistance R_L. As indicated in Fig. 3, R_{ct}, R_{diff} and $Y_{C_{diff}}$ can be summed up to the cathodic impedance Z_C, L and R_L to the anodic impedance Z_A.[39] According to King *et al.*,[38] the corrosion rate is inversely proportional to the polarization resistance R_P. R_P corresponds to the impedance at zero frequency and reads therefore:

$$\frac{1}{R_P} = \frac{1}{R_C} + \frac{1}{R_A} \quad (1)$$

$$\text{with } \frac{1}{R_C} = \frac{1}{R_{ct} + R_{diff}} \text{ and } R_A = R_L,$$

where R_A and R_C denote the anodic and cathodic resistance, respectively.

Table 1 shows the various parameters which are deduced from fitting the measured spectra (Fig. 2) with the EEC of Fig. 3. The obtained fit parameters are in the following analysed according to Baril *et al.*,[36] or Liu *et al.*[39] The smaller charge transfer resistance R_{ct} fitted for $ZX00_{HPT}$, as compared to $ZX00_{EXT}$, corresponds directly to the hardly pronounced high frequency loop in Fig. 2. The smaller value of $Y_{C_{int}}$ for $ZX00_{HPT}$ indicates a smaller fraction of MgO formed on the sample surface. Together with the smaller R_{ct} value, this points towards a lack of protection from the oxide layer after HPT deformation. Since $n_{C_{int}}$ is smaller than 1 for both samples, deviations from an ideal capacitive behavior can be assumed and attributed to some inhomogeneities on the surface.[16] The smaller R_{diff} value fitted for $ZX00_{HPT}$ indicates a decreased resistance of the corrosion product layer against the diffusion of Mg^{2+} and therefore points towards a less compact corrosion layer formed after HPT deformation. As shown in Table 2, the significantly decreased R_P value indicates, according to King *et al.*,[38] an enhanced corrosion rate for $ZX00_{HPT}$. Furthermore a more dominating anodic activity can be observed due to the decreased R_A value after HPT processing leading to a faster dissolution of $ZX00_{HPT}$ as compared to $ZX00_{EXT}$.

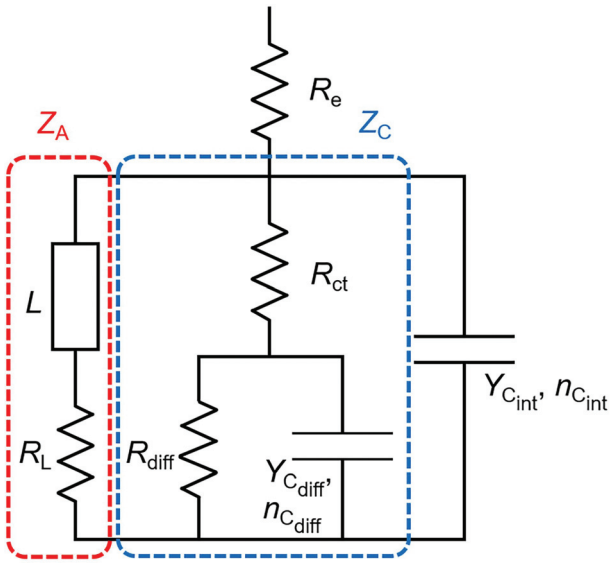

Fig. 3 Equivalent electrical circuit used for fitting the measured electrochemical impedance spectra in Fig. 2. Parameters (for results see Table 1): anodic impedance Z_A consisting of the inductance L and the resistance R_L to fit the inductive behavior in the low frequency range. Cathodic impedance Z_C consisting of the charge transfer resistance R_{ct} associated with hydrogen evolution and the resistance R_{diff} with the constant phase element $Y_{C_{diff}}$ with $n_{C_{diff}}$ ascribed to the diffusion of Mg^{2+} through the $Mg(OH)_2$ layer. R_e denotes the electrolyte resistance and $Y_{C_{int}}$ with $n_{C_{int}}$ the constant phase element used to fit the capacitance of the MgO film.

Table 1 Characteristic values deduced from the measured impedance spectra (Fig. 2) by means of fitting the equivalent electrical circuit (EEC) shown in Fig. 3. The EEC elements are defined in the caption of Fig. 3

	L (H cm^2)	R_L (Ω cm^2)	$Y_{C_{diff}}$ (μs cm^{-2})	$n_{C_{diff}}$	R_{diff} (Ω cm^2)
$ZX00_{EXT}$	37 339	2833	3086	0.98	197
$ZX00_{HPT}$	273	21	32	0.98	47
	R_e (Ω cm^2)	R_{ct} (Ω cm^2)	$Y_{C_{int}}$ (μs cm^{-2})	$n_{C_{int}}$	
$ZX00_{EXT}$	19	585	41	0.86	
$ZX00_{HPT}$	14	10	17	0.89	

Table 2 Polarization resistance R_P, cathodic resistance R_C, and anodic resistance R_A according to eqn (1) obtained from the fit values given in Table 1

	R_C (Ω cm^2)	R_A (Ω cm^2)	R_P (Ω cm^2)
$ZX00_{EXT}$	782	2833	613
$ZX00_{HPT}$	57	21	15

C. Positron lifetime measurements

The results of the e^+ lifetime measurements are summarized in Table 3. For pure, annealed Mg a single e^+ lifetime τ_1 = 226 ps is found which represents the e^+ bulk lifetime in Mg (see Discussion and Table 4).

In the *uncorroded states* of $ZX00_{EXT}$ and $ZX00_{HPT}$, mean e^+ lifetimes τ_m of 232 ps and 241 ps are found, respectively. A two-component analysis reveals for $ZX00_{EXT}$ the trap component τ = 254 ps with an intensity of 58.9% which will be attributed to e^+ trapping and annihilation in grain boundaries (GBs) of the extruded sample (see Discussion). The uncorroded state of $ZX00_{HPT}$ can be well described by a single e^+ lifetime component, presumably because the fraction of e^+ annihilating in the free bulk state cannot be resolved due to strong e^+ trapping. In fact, a two-component analysis with the trap component τ = 254 ps, found for $ZX00_{EXT}$, being fixed yields a high trap intensity I_2 = 75.2% for $ZX00_{HPT}$.

The e^+ lifetime measurements reveal substantial differences in the *corrosion behavior* of $ZX00_{EXT}$ and $ZX00_{HPT}$ as demonstrated by their different variations of τ_m with corrosion time t_{corr} (see Fig. 4). For $ZX00_{HPT}$, τ_m starts to increase after 60 s of corrosion already, whereas for $ZX00_{EXT}$ faint changes can be discerned only after 5 min. Particular pronounced differences occur with prolonged corrosion of 2 h and longer, where τ_m of $ZX00_{HPT}$ strongly increases, by nearly 80 ps in total up to 48 h of corrosion, in contrast to $ZX00_{EXT}$ which exhibits a total τ_m-increase of 7 ps only.

According to e^+ lifetime spectroscopy, a trap component with long e^+ lifetime exceeding 500 ps emerges for $ZX00_{HPT}$ after 60 s and for $ZX00_{EXT}$ after 5 min of corrosion (Table 3). The components τ_1 and τ_2 can no longer be separated for $ZX00_{EXT}$ when the long component emerges (see, *e.g.*, the data set for 25 min and 48 h). Therefore, the GB component τ_2 = 254 ps had to be fixed. To minimize the numerical uncertainties associated with the small intensity of the long component τ_3, also this component was fixed to the value of 903 ps found in the unconstrained two-component analysis of the spectrum with t_{corr} = 25 min. The intensity I_3 of the long component deduced in this way exhibits a maximum value of 1.2%. For $ZX00_{HPT}$, the intensity of the long component increases more strongly and even a second long component exceeding 500 ps is found for $t_{corr} \geq 10$ h. For comparison of $ZX00_{EXT}$ and $ZX00_{HPT}$, the variation of the intensity I_3 of the long com-

Table 4 Positron lifetimes in free state (τ_b) and defect-trapped state in vacancy (τ_v) and dislocation (τ_d) in pure Mg according to literature. Experimental values unless stated

τ_b (ps)	225	Hautojärvi *et al.*[56]
	225	Čížek *et al.*[57]
	226	Dryzek *et al.*[58]
	233	Čížek *et al.*,[57] theoretical
	237	Puska and Nieminen,[19] theoretical
τ_v (ps)	255	Hautojärvi *et al.*[56]
	297	Čížek *et al.*,[57] theoretical
	307	Nieminen and Manninen,[59] theoretical
τ_d (ps)	256	Čížek *et al.*[41]
	257	Čížek *et al.*[41]

Table 3 Results of positron lifetime spectroscopy of $ZX00_{EXT}$ and $ZX00_{HPT}$ along with the relative change $\Delta m/m_0$ of the sample mass in dependence of corrosion time t_{corr}: mean e^+ lifetime $\tau_m = \Sigma_i I_i \tau_i$ and e^+ lifetime components τ_i with relative intensities I_i (i = 1, 2, 3); value in bracket: numerical uncertainty, fix: component fixed for analysis. The result obtained for pure annealed Mg is given for comparison

t_{corr}	τ_1 (ps)	I_1 (%)	τ_2 (ps)	I_2 (%)	τ_3 (ps)	I_3 (%)	τ_m (ps)	$\Delta m/m_0$
$ZX00_{EXT}$								
0 s	201(22)	41.1(35.8)	254(17)	58.9(35.8)			232	
12 s	198(4)	40.3(3.2)	254(fix)	59.7(3.2)			231	
60 s	190(4)	34.3(2.3)	254(fix)	65.7(2.2)			232	0.0000
5 min	210(4)	52.2(5.5)	254(fix)	47.4(5.6)	903(fix)	0.4(0.1)	233	0.0003
25 min	229(1)	98.8(0.2)			903(79)	1.2(0.2)	237	
25 min	212(5)	56.4(7.7)	254(fix)	42.6(7.7)	903(fix)	1.0(0.1)	236	0.0023
2 h	211(5)	56.1(7.6)	254(fix)	42.9(7.7)	903(fix)	1.0(0.1)	236	0.0029
10 h	206(5)	47.0(5.5)	254(fix)	52.6(5.6)	903(fix)	0.4(0.1)	234	0.0036
24 h	212(5)	55.4(6.6)	254(fix)	44.0(6.6)	903(fix)	0.6(0.1)	235	0.0057
48 h	229(1)	98.5(0.2)			886(65)	1.5(0.2)	239	
48 h	210(6)	52.9(7.2)	254(fix)	45.9(7.2)	903(fix)	1.2(0.1)	239	0.0047
$ZX00_{HPT}$								
0 s	241(1)	100.0					241	
0 s	203(7)	24.8(3.4)	254(fix)	75.2(3.4)			241	
12 s	241(1)	100.0					241	
60 s	240(1)	99.6(0.1)			1500(206)	0.4(0.1)	245	0.0000
5 min	240(1)	99.7(0.1)			2180(429)	0.3(0.1)	247	0.0005
25 min	241(1)	99.1(0.1)			1663(129)	0.9(0.1)	254	0.0036
2 h	242(1)	99.0(0.1)			1408(89)	1.0(0.1)	254	0.0074
10 h	242(1)	94.8(0.6)	686(82)	4.4(0.5)	2514(688)	0.8(0.2)	279	−0.0089
24 h	242(1)	92.6(0.5)	687(47)	6.2(0.3)	2052(290)	1.2(0.3)	290	−0.0720
48 h	239(2)	85.0(1.5)	573(52)	12.0(1.1)	1590(157)	3.0(0.6)	319	−0.1490
Mg								
0 s	226(1)	100.0					226	

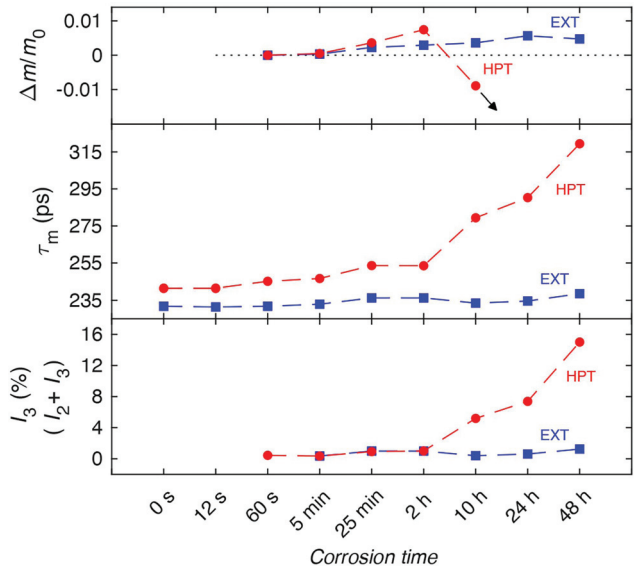

Fig. 4 Results of positron lifetime spectroscopy of $ZX00_{EXT}$ (blue) and $ZX00_{HPT}$ (red) along with the relative change $\Delta m/m_0$ of the sample mass in dependence of corrosion time t_{corr}: Mean e^+ lifetime τ_m; Intensity I_3 or $I_2 + I_3$ of long e^+ lifetime components ($\tau_{2,3} > 500$ ps, $I_2 + I_3$ refers to the intensity sum for $t_{corr} \geq 10$ h of $ZX00_{HPT}$). Complete data set and numerical uncertainties see Table 3.

ponent, respectively the sum $I_2 + I_3$ of the two long components in $ZX00_{HPT}$ for $t_{corr} \geq 10$ h, is shown in Fig. 4.

Finally, we note that the component τ_1 found for $ZX00_{HPT}$ in the analysis of the spectra after corrosion has to be considered as averaged value between the trap component $\tau = 254$ ps and the annihilation in the bulk which cannot be resolved as outlined above for the spectrum of the uncorroded state of $ZX00_{HPT}$.

Supplementary to the e^+ annihilation measurements, after each corrosion step the mass m of each sample pair was determined in order to assess the fraction of corroded material evolved on the sample surfaces. The relative mass variation $\Delta m/m_0$ for the two sample sets $ZX00_{EXT}$ and $ZX00_{HPT}$ with corrosion time is shown in Table 3 and Fig. 4. Both samples show a pretty similar increase of $\Delta m/m_0$ up to 2 h. Upon continuing corrosion, $\Delta m/m_0$ of $ZX00_{EXT}$ further increases up to 24 h, whereas that of $ZX00_{HPT}$ strongly decreases. This is due to a peeling off of the corrosion product.

From the increase of $\Delta m/m_0$, an estimate can be given on the fraction of positrons expected to be stopped in the corrosion layer. For simplicity, it is assumed that as single corrosion product a $Mg(OH)_2$ layer is formed at the surface. The sample mass is therefore given by:

$$m = m_{Mg} + m_{Mg(OH)_2} = (m_0 - xM_{Mg}) + x(M_{Mg} + 2M_H + 2M_O) = m_0 + 2x(M_H + M_O), \quad (2)$$

where x denotes the number of moles of corroded Mg, m_0 the initial mass, m_{Mg} and $m_{Mg(OH)2}$ the mass of Mg and the $Mg(OH)_2$-layer, respectively, and M_H, M_O and M_{Mg} the mole mass of hydrogen, oxygen and magnesium, respectively. From eqn (2) the mass of the corrosion product layer:

$$m_{Mg(OH)_2} = \frac{(m - m_0)(M_{Mg} + 2M_H + 2M_O)}{2(M_H + M_O)} \quad (3)$$

and its thickness:

$$d_{Mg(OH)_2} = \frac{m_{Mg(OH)_2}}{\rho_{Mg(OH)_2} A} \quad (4)$$

follows with the density $\rho_{Mg(OH)2} = 2.34$ g cm^{-3} (ref. 40) and the sample area A. From the area density $m_{Mg(OH)2}A^{-1} = \rho_{Mg(OH)2} d_{Mg(OH)2}$ of the $Mg(OH)_2$ layer, the fraction of e^+ beeing stopped in the layer can be calculated as follows:[17]

$$f_{e^+,corr} = 1 - \exp\left(-\frac{\rho_{Mg(OH)_2} d_{Mg(OH)_2}}{25\ \text{mg cm}^{-2}}\right). \quad (5)$$

Assuming that the e^+ diffusion length in the corrosion layer is small due to a high defect density, $f_{e^+,corr}$ also corresponds to the fraction of e^+ beeing annihilated in this layer.

The increase of $d_{Mg(OH)_2}$ and $f_{e^+,corr}$ with corrosion time deduced from the measured mass increase $\Delta m/m_0$ of $ZX00_{EXT}$ is shown in Fig. 5. For the initial mass m_0, the sample mass after 60 s is used as no change in e^+ annihilation data up to 5 min of corrosion could be observed. A maximum corrosion layer thickness of *ca.* 4 μm with a corresponding maximum fraction $f_{e^+,corr}$ of *ca.* 3% is estimated.

IV. Discussion

A. Open-volume defects prior to corrosion

We start the discussion with a consideration of the characteristic e^+ lifetime in the Mg alloy and the type of open-volume defects in the extruded ($ZX00_{EXT}$) and HPT-deformed ($ZX00_{HPT}$) state prior to corrosion. The literature value $\tau_b = 225/6$ ps reported for the bulk e^+ lifetime in the defect-free state of Mg (Table 4) could be well reproduced in the present study (Table 3). For e^+ annihilation at dislocations values of

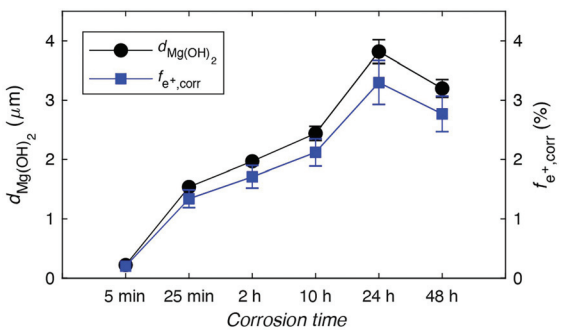

Fig. 5 Thickness $d_{Mg(OH)_2}$ of corrosion product layer (eqn (4)) and fraction $f_{e^+,corr}$ of e^+ being stopped in the layer (eqn (5)) in dependence of corrosion time deduced from the measured mass increase $\Delta m m_0^{-1}$ of $ZX00_{EXT}$.

256/7 ps are reported by Čížek *et al.*[41] similar to the trap component τ_2 = 254 ps found here for $ZX00_{EXT}$. This trap component is considered to arise from e^+ trapping and annihilation in grain boundaries of the recrystallized microstructure. Positron lifetimes similar to that of dislocations and smaller than that of lattice vacancies (Table 4) are typical for GBs.

The assignment of τ_2 to GBs is further supported by quantitatively considering the intensity of the e^+ annihilation component which is expected for trapping at grain boundaries (GBs) and matrix–precipitate interfaces based on the microstructural parameters quoted in section III A. For this purpose, our models of diffusion- and reaction-limited e^+ trapping at the aforementioned defect types[42–45] were applied by making use of the solutions which are summarized in the appendix. The used e^+ annihilation parameters are quoted in Table 5, among them are the bulk e^+ lifetime τ_b = 226 ps measured on annealed Mg and the trap lifetime component $\tau_{gb,if}$ = 254 ps observed for $ZX00_{EXT}$, which is considered as the e^+ lifetime component in grain boundaries or precipitate–matrix interfaces. Using these parameters, the mean e^+ lifetime τ_m and the intensities of the e^+ annihilation component in grain boundaries (I_{gb}) and matrix–precipitate interfaces (I_{if}) are calculated for spherical- or cylindrical-shaped grains with various radii r as well as for spherical-shaped precipitates using as radius r and half distance R between precipitates the typical values reported for the intermetallic particles in a similar Mg–Zn–Ca alloy. The results are summarized in Table 5.

The model with e^+ trapping at GBs of spherical-shaped grains with diameter of 2 μm describes the measuring data for $ZX00_{EXT}$ remarkably well; the intensity I_{gb} = 63% of the e^+ annihilation component in GBs and the mean e^+ lifetime τ_m = 233 ps are close to the experimental values (I_2 = 59%, τ_m = 232 ps; Table 4). Likewise the experimental results for $ZX00_{HPT}$ can be well described by e^+ trapping at GBs of cylindrical-shaped grains with diameter of 1 μm, as a comparison of the e^+ annihilation component in GBs according to this model (76%, Table 5) with the result from spectra analysis (I_2 = 75%, Table 3) shows. The higher experimental τ_m-value compared to the model may indicate that the experimental e^+ lifetime component τ_1 does not exclusively reflect e^+ annihilation in the free bulk state.

The interfaces between precipitates and matrix, on the other hand, contribute only to a minor extent to e^+ trapping: a small trap intensity I_{if} = 2.2% is predicted for an interparticle distance of 1.5 μm between precipitates with diameter of 80 nm (Table 5). Fragmentation of the precipitates during HPT-processing might increase this contribution for $ZX00_{HPT}$, however, also e^+ trapping at GBs is stronger in that case, compared to $ZX00_{EXT}$, due to the smaller grain size.

B. Corrosion behaviour

In the following section the substantially different corrosion behavior of $ZX00_{EXT}$ and $ZX00_{HPT}$ as revealed by the complementary e^+ annihilation and electrochemical impedance measurements will be discussed. EIS is highly surface sensitive and therefore allows the investigation of the evolving corrosion product layer.[29] In contrast, by using conventional positron sources, as done in this work, the materials bulk can be investigated with a high sensitivity of about 1 to 100 atomic ppm towards defects in the sub-nanometer range.[17–19] As a result, also corrosion-related changes in the materials bulk can be monitored. Therefore a more global picture of the corrosion processes can be given by combining EIS with bulk sensitive PLS measurements. To the authors knowledge, such a combination of these two measurements techniques has not been used so far for studying the corrosion process of Mg alloys.

At first the results of electrochemical impedance spectroscopy will be discussed. For this purpose and the sake of illustration, a scheme of the corrosion-induced prospective microstructure is shown in Fig. 6. The corrosion products form a loosely bonded filamentous layer consisting of $Mg(OH)_2$, $MgCO_3$ and $Ca_{10}(PO_4)_6(OH)_2$.[35,40,46] Between this corrosion product layer and the alloy, there is a thin and more dense oxide interlayer of MgO, where cracks can emerge in the

Table 5 Intensity of e^+ annihilation component in grain boundaries (I_{gb}) or interfaces (I_{if}) with respective mean e^+ lifetime τ_m according to diffusion-reaction trapping models for spherical- or cylindrical-shaped grains and for precipitate–matrix interface of spherical-shaped precipitates. The model solutions are summarized in the appendix. Parameters: r: grain or precipitate radius, R: half distance between precipitates; D: e^+ diffusivity, α: specific e^+ trapping rate at interface, τ_b: e^+ bulk lifetime: τ_{gb}, τ_{if}: e^+ lifetime in grain boundary or precipitate–matrix interface, respectively. The value r for precipitates is chosen according to literature;[35] for α see, *e.g.*, references in 44

Spherical grain	r (μm)		τ_m (ps) (eqn A1)	I_{gb} (%) (eqn A3)
	0.5		239	85
	1.0		233	63
	1.5		231	48
Cylindrical grain	r (μm)		τ_m (ps) (eqn A2)	I_{gb} (%) (eqn A4)
	0.5		235	76
Precipitate–matrix interface	r (nm)	R (nm)	τ_m(ps) (eqn A8)	I_{if} (%) (eqn A9)
	40 [35]	750	226	2.2
Model parameters	D (m^2 s^{-1})	α (ms^{-1})	τ_b (ps)	$\tau_{gb,if}$ (ps)
	5×10^{-5} (ref. 60)	3000	226	254

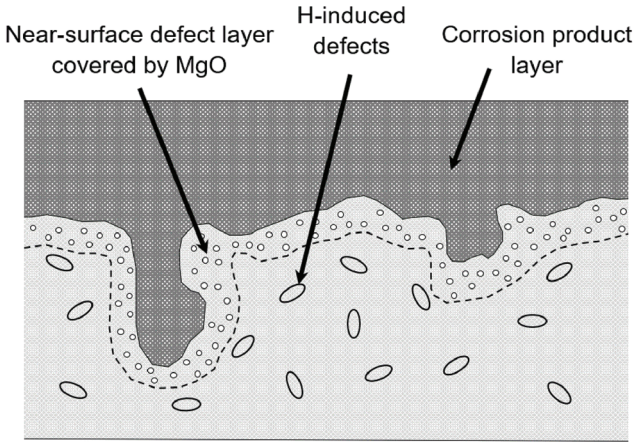

Fig. 6 Corrosion creates a near-surface defect layer in the alloy, which is covered by a thin MgO layer, followed by further corrosion products. Deeper inside the alloy bulk, hydrogen induced defects may form.

course of corrosion.[40] The nanometric intermetallic particles, composed of the Laves-type Mg_2Ca phase (see section III A), dissolve with no observable remnants in the corrosion products, as found by electron microscopy studies.[35]

The impedance spectrum of $ZX00_{HPT}$ strongly differs from that of $ZX00_{EXT}$ with respect to both size and shape (Fig. 2). For $ZX00_{HPT}$, the generally smaller spectrum and in particular the strongly reduced polarization resistance R_P (Table 2), which is inversely proportional to the corrosion rate, indicates a decreased corrosion resistance of this sample type. This faster dissolution can be considered to arise from the higher density of structural defects, especially grain boundaries, present in the HPT-processed material, leading to a less protective surface product film, as supported by the decreased R_{diff} value (Table 1). As known from literature,[10] a fast formation of the porous $Mg(OH)_2$ layer will not effectively create a barrier between the alloy matrix and the corrosive electrolyte. The high dissolution activity at HPT-induced defects will cause extensive hydrogen formation, which leads to cracks, disruptions and delamination in the $Mg(OH)_2$ layer. These imperfections in the $Mg(OH)_2$ layer provide channels for the electrolyte to reach the surface and thus increase the film-free surface area, leading to the high dissolution activity and the significant decrease in the anodic resistance R_A.

This interpretation is also supported by the characteristic shapes of the different EIS spectra: the $ZX00_{EXT}$ spectrum consists of two clear capacitive loops (upper branch), with the high frequency (left) loop stemming from charge transfer across the interface in parallel to the MgO film capacitance and the low frequency (right) loop representing Mg^{2+} transport through the porous surface layer, and one inductive loop (lower branch) caused by Mg^+ intermediates at the surface and thus indicating direct dissolution from alloy into the electrolyte.[36] In contrast to this, in the $ZX00_{HPT}$ spectrum, the high frequency loop is hardly existent, only visible as a small shoulder, while the inductive loop is more pronounced, both indicating the lack of an effectively protective corrosion product layer.

The reduced corrosion resistance of HPT-processed samples, as deduced from EIS, strongly affects the open-volume defects which evolve during corrosion as observed by e^+ lifetime spectroscopy. The estimated fraction $f_{e^+,corr}$ of positrons beeing stopped in the corrosion product layer (Fig. 5) up to a corrosion time of 2 h is rather similar to the measured intensity I_3 of the e^+ lifetime component τ_3 for both $ZX00_{EXT}$ and $ZX00_{HPT}$. The component τ_3 can therefore be attributed to e^+ annihilation in this product layer and the oxide layer underneath. The high value of τ_3, exceeding 500 ps, is characteristic for positronium formation and annihilation in larger open-volume structures such as pores and cracks. This direct proof for larger open-volume elements supports the notion on the defect structure obtained by other techniques, such as transmission electron microscopy, small angle neutron scattering, or gas adsorption.[40] These studies reveal for the corrosion product layer a nanoporous filamentous structure with pore sizes ranging from 20 to 40 nm. The MgO interlayer, on the other hand, is considered to affect e^+ annihilation only to a minor extent if at all. According to studies of different Mg alloys in corrosive environments, the thickness of this layer is in the range of a few hundred nanometers or even less, *i.e.*, much thinner than the corrosion product layer.[37,40]

The earlier onset of the τ_3-component and its higher value in $ZX00_{HPT}$ (after 60 s, already) compared to $ZX00_{EXT}$ (after 5 min, only) indicate a more stronger onset of corrosion after HPT as also clearly shown by the present results from EIS (Fig. 2). The substantially reduced resistance of $ZX00_{HPT}$ against corrosion observed by EIS becomes more dramatically effective in the defect structure formed after longer corrosion times t_{corr} >2 h. The intensity sum $I_2 + I_3$ of the long e^+ annihilation components strongly exceeds the fraction $f_{e^+,corr}$ of e^+ beeing stopped in the corrosion product layer (compare Fig. 4 and Fig. 6). This is considered as clear evidence for corrosion-induced defects with large open volume in deeper parts of the $ZX00_{HPT}$-material.

The enhanced corrosion rate favors void formation within the matrix underneath the surface Mg-oxide forming a defect-rich layer.[23] Of even more relevance here is the fact that the major corrosion product, namely hydrogen, can be absorbed during degradation by the Mg matrix[20,21] and may induce defects in far deeper parts. For instance, electron microscopy in combination with secondary ion mass spectroscopy yields evidence of cracks in the μm-range during corrosion as a result of the brittle fracture of MgH_2.[20] Also, stress corrosion cracking tests suggest hydrogen embrittlement caused, *e.g.*, by crack formation.[21] In coarse-grained metals upon hydrogen loading evidence for large open-volume defects is found in near surface regions by positron annihilation,[47,48] but not for the bulk where vacancy-type defects and dislocations prevail as e^+ traps.[49,50] Fine-grained HPT-deformed Mg, on the other hand, is strongly absorbing hydrogen into the bulk, presumably arising from enhanced diffusivity associated with the high number of GBs.[51] Furthermore, a faster corrosion process is accompanied by an enhanced production of hydrogen,[29] leading to a larger amount of absorbable hydrogen. We therefore conclude that the strong hydrogen uptake during cor-

rosion into the bulk of $ZX00_{HPT}$ combined with the reduced corrosion resistance (monitored by EIS) and the larger amount of absorbable hydrogen gives rise to the formation of large open-volume defects in deeper parts which is detected in the present study by the strong intensity increase the long e^+ annihilation components.

In contrast, the intensity I_3 of $ZX00_{EXT}$ does not exceed the fraction $f_{e^+,corr}$ of e^+ beeing stopped in the corrosion product layer for longer corrosion times t_{corr} >2 h and the τ_3 component can still be related to annihilation events mainly in the corrosion product layer. Corrosion-related defects deeper into the material are not detected during the investigated corrosion time, which is in good accordance with the slower corrosion rate, as found by EIS. Therefore it can be concluded, that further grain refinement and the so additionally introduced defects, as *e.g.* done in this work by HPT processing, has negative effects on the corrosion behavior of the investigated ZX00 alloy and makes it less suitable for potential biomedical application. Corrosion-dampening strategies, which were successfully applied to Mg-alloys in the past,[52] might be an addition of Mn, which can be tolerated by the human body and is known to mitigate impurity-effects on corrosion, or also a pre-anodization treatment of the samples to delay the onset of corrosion. Beside the choice of a suitable material, also the physiological environment has an effect on the samples degradation behavior. Adding biological ions or proteins to the corrosive environment, *e.g.*, causes changes in the degradation morphology due to an enhanced pit formation on the materials surface.[53] Therefore adding some proteins to PBS, *e.g.*, will provide further insights into the corrosion behavior of ZX00 alloys with respect to the use in the human body.

V. Conclusion

In this work positron lifetime and electrochemical impedance spectroscopy were successfully applied to investigate the corrosion process of a Mg-based alloy. In good agreement with electrochemical impedance spectroscopy, PLS shows that HPT-processing clearly reduces the corrosion resistance of the here-investigated Mg-based alloy ZX00. We see that severe plastic deformation introduces significant amounts of open volume defects, especially grain boundaries, into the uncorroded material, which in the following strongly influence the degradation behavior. For HPT-samples, structural defects such as cracks and voids formed within the corrosion product layer, making this layer ineffective in protecting the surface from further corrosion and leading together with the higher grain boundary density to enhanced corrosion rates. In addition, the HPT-deformed structure also favors hydrogen-uptake into the material, causing large open-volume defects in deeper parts of the material below the corrosion layer, as shown by positron annihilation, and leading to a further deterioration of the materials properties.

Further combination of positron lifetime measurements with an appropriate electrochemical cell, as demonstrated recently for battery electrodes,[54] would allow to study dynamically and *in situ* the corrosion process under cathodic or anodic polarization, *e.g.*, and would give further insights in the formation of corrosion-related defects.

Conflicts of interest

There are no conflicts of interest to declare.

A. Results of diffusion-reaction models of positron trapping at extended defects

Diffusion- and reaction limited e^+ trapping at grain boundaries has been treated by Würschum and Seeger[42] and by Oberdorfer and Würschum[43] for spherical-shaped grains and by Würschum[45] for cylindrical-shaped grains.

The mean e^+ lifetime reads for spherical symmetry (ref. 43, eqn (30)):

$$\tau_m = \tau_b\left\{1 + \frac{3\alpha}{r}(\tau_{gb} - \tau_b)\frac{\gamma_0 DL(\gamma_0 r)}{\alpha + \gamma_0 DL(\gamma_0 r)}\right\} \quad (A1)$$

and for cylindrical symmetry (ref. 45: left part of eqn (10) without weighting factor $(r/R)^2$):

$$\tau_m = \tau_b\left\{1 + \frac{2\alpha}{r}(\tau_{gb} - \tau_b)\frac{\gamma_0 D\Theta(\gamma_0 r)}{\alpha + \gamma_0 D\Theta(\gamma_0 r)}\right\}. \quad (A2)$$

The intensity of the e^+ lifetime component τ_{gb} associated with trapping and annihilation at GBs reads for spherical symmetry (ref. 43, eqn (31)):

$$I_{gb} = \frac{3\alpha}{r}\frac{\gamma_{gb} DL(\gamma_{gb} r)}{[\alpha + \gamma_{gb} DL(\gamma_{gb} r)](\tau_b^{-1} - \tau_{gb}^{-1})} \quad (A3)$$

and for cylindrical symmetry (ref. 45: eqn (16) without weighting factor $(r/R)^2$):

$$I_{gb} = \frac{2\alpha}{r}\frac{\gamma_{gb} D\Theta(\gamma_{gb} r)}{[\alpha + \gamma_{gb} D\Theta(\gamma_{gb} r)]\left(\tau_b^{-1} - \tau_{gb}^{-1}\right)}, \quad (A4)$$

with

$$\gamma_0^2 = \frac{\tau_b^{-1}}{D}, \quad \gamma_{gb}^2 = \frac{\tau_b^{-1} - \tau_{gb}^{-1}}{D}, \quad (A5)$$

the Langevin function:

$$L(z) = \coth z - \frac{1}{z} \quad (A6)$$

and

$$\Theta(z) = \frac{I_1(z)}{I_0(z)}, \quad (A7)$$

where I_j (j = 0, 1) denote the modified Bessel functions.[55] D denotes the e^+ diffusivity, α the specific e^+ trapping rate, τ_{gb} the e^+ lifetime in the grain boundary, and r the grain radius.

Solutions for diffusion- and reaction limited e^+ trapping at precipitate–matrix interfaces of spherical-shaped precipitates were presented by Würschum *et al.*[44] The mean e^+ lifetime reads (ref. 44: eqn (30)):

$$\tau_m = \tau_b \left\{ 1 + K(\tau_{if} - \tau_b) \frac{\gamma_0 \hat{R} - \tanh(\gamma_0 \hat{R})[1 - \gamma_0^2 rR]}{\gamma_0 \hat{R} - \tanh(\gamma_0 \hat{R})[1 - \gamma_0^2 rR] + \frac{\alpha r}{D}[\gamma_0 R - \tanh(\gamma_0 \hat{R})]} \right\} \quad \text{(A8)}$$

and the intensity of the e^+ lifetime component τ_{if} associated with trapping and annihilation at the precipitate–matrix interface (ref. 44: eqn (31)):

$$I_{if} = \frac{K}{\tau_b^{-1} - \tau_{if}^{-1}} \frac{\gamma_{if} \hat{R} - \tanh(\gamma_{if} \hat{R})[1 - \gamma_{if}^2 rR]}{\gamma_{if} \hat{R} - \tanh(\gamma_{if} \hat{R})[1 - \gamma_{if}^2 rR] + \frac{\alpha r}{D}[\gamma_{if} R - \tanh(\gamma_{if} \hat{R})]} \quad \text{(A9)}$$

with

$$\gamma_{if}^2 = \frac{\tau_b^{-1} - \tau_{if}^{-1}}{D}, \quad K = \frac{3\alpha r^2}{R^3 - r^3}, \quad \hat{R} = R - r, \quad \text{(A10)}$$

where R denotes the half distance between the precipitates and r the precipitate radius.

Acknowledgements

The authors are indebted to Wolfgang Sprengel (Institute of Materials Physics, TU Graz) for technical support and for valuable comments.

References

1 P. Holweg, L. Berger, M. Cihova, N. Donohue, B. Clement, U. Schwarze, N. G. Sommer, G. Hohenberger, J. J. van den Beucken, F. Seibert, *et al.*, *Acta Biomater.*, 2020, **113**, 646–659.
2 H. Ibrahim, A. D. Klarner, B. Poorganji, D. Dean, A. A. Luo and M. Elahinia, *J. Mech. Behav. Biomed. Mater.*, 2017, **69**, 203–212.
3 B. J. Luthringer, F. Feyerabend and R. Willumeit-Römer, *Magnesium Res.*, 2014, **27**, 142–154.
4 G. Manivasagam and S. Suwas, *Mater. Sci. Technol.*, 2014, **30**, 515–520.
5 N. Li and Y. Zheng, *J. Mater. Sci. Technol.*, 2013, **29**, 489–502.
6 H. Zreiqat, C. Howlett, A. Zannettino, P. Evans, G. Schulze-Tanzil, C. Knabe and M. Shakibaei, *J. Biomed. Mater. Res.*, 2002, **62**, 175–184.
7 N. G. Grün, P. Holweg, S. Tangl, J. Eichler, L. Berger, J. J. Van den Beucken, J. F. Löffler, T. Klestil and A. M. Weinberg, *Acta Biomater.*, 2018, **78**, 378–386.
8 N. Ikeo, M. Nishioka and T. Mukai, *Mater. Lett.*, 2018, **223**, 65–68.
9 J. Horky, A. Ghaffar, K. Werbach, B. Mingler, S. Pogatscher, R. Schäublin, D. Setman, P. J. Uggowitzer, J. F. Löffler and M. J. Zehetbauer, *Materials*, 2019, **12**, 2460.
10 D. Song, A. Ma, J. Jiang, P. Lin, D. Yang and J. Fan, *Corros. Sci.*, 2010, **52**, 481–490.
11 C. op't Hoog, N. Birbilis and Y. Estrin, *Adv. Eng. Mater.*, 2008, **10**, 579–582.
12 M. Gholami-Kermanshahi, V.-D. Neubert, M. Tavakoli, F. Pastorek, B. Smola and V. Neubert, *Adv. Eng. Mater.*, 2018, **20**, 1800121.
13 J. Gao, S. Guan, Z. Ren, Y. Sun, S. Zhu and B. Wang, *Mater. Lett.*, 2011, **65**, 691–693.
14 D. Ahmadkhaniha, Y. Huang, M. Jaskari, A. Järvenpää, M. H. Sohi, C. Zanella, L. P. Karjalainen and T. G. Langdon, *J. Mater. Sci.*, 2018, **53**, 16585–16597.
15 C. Zhang, S. Zhu, L. Wang, R. Guo, G. Yue and S. Guan, *Mater. Des.*, 2016, **96**, 54–62.
16 Y. Xu, J. Li, M. Qi, J. Gu and Y. Zhang, *J. Mater. Sci.*, 2020, **55**, 1231–1245.
17 P. Hautojärvi, A. Dupasquier and M. Manninen, *Positrons in solids*, Springer, 1979, vol. 12.
18 R. Krause-Rehberg and H. S. Leipner, *Positron annihilation in semiconductors: defect studies*, Springer Science and Business Media, 1999, vol. 127.
19 M. J. Puska and R. M. Nieminen, *Rev. Mod. Phys.*, 1994, **66**, 841.
20 J. Chen, J. Wang, E. Han, J. Dong and W. Ke, *Corros. Sci.*, 2008, **50**, 1292–1305.
21 M. Kappes, M. Iannuzzi and R. M. Carranza, *J. Electrochem. Soc.*, 2013, **160**, C168.
22 W. Yang, Z. Zhu, J. Wang, Y. Wu, T. Zhai and G.-L. Song, *Corros. Sci.*, 2016, **106**, 271–280.
23 Y. Wu, R. Zhang, H. Chen, Y. Li, J. Zhang, D.-M. Zhu and Y. Jean, *Radiat. Phys. Chem.*, 2003, **68**, 599–603.
24 X. Wu, P. Asoka-Kumar, K. Lynn and K. R. Hebert, *J. Electrochem. Soc.*, 1994, **141**, 3361.
25 R. Pietrzak, R. Szatanik and M. Szuszkiewicz, *Acta Phys. Pol., A*, 1999, **95**, 647–651.
26 R. Pietrzak and R. Szatanik, *Phys. Status Solidi B*, 2010, **247**, 1822–1828.
27 R. Pietrzak and R. Szatanik, *Nukleonika*, 2015, **60**, 755–758.
28 M. R. E. S. Aly, H. Shokry, T. Sharshar and M. A. Amin, *J. Mol. Liq.*, 2016, **214**, 319–334.
29 N. Kirkland, N. Birbilis and M. Staiger, *Acta Biomater.*, 2012, **8**, 925–936.
30 H. Schröttner, *Gießerei-Praxis*, 2010, **10**, 307–320.
31 T. Pabel, T. Petkov, H. Schröttner, M. Albu, A. Rossmann-Perner and P. Schumacher, 57th International Foundry Conference, 2017, p. 93.

32 D. J. Keeble, U. Brossmann, W. Puff and R. Würschum, *Charact. Mater.*, 2002, 1–28.
33 J. V. Olsen, P. Kirkegaard, N. J. Pedersen and M. Eldrup, *Phys. Status Solidi C*, 2007, **4**, 4004–4006.
34 O. Poupard, A. Aït-Mokhtar and P. Dumargue, *J. Mater. Sci.*, 2003, **38**, 2845–2850.
35 M. Cihova, E. Martinelli, P. Schmutz, A. Myrissa, R. Schäublin, A. M. Weinberg, P. Uggowitzer and J. F. Löffler, *Acta Biomater.*, 2019, **100**, 398–414.
36 G. Baril, G. Galicia, C. Deslouis, N. Pébère, B. Tribollet and V. Vivier, *J. Electrochem. Soc.*, 2006, **154**, C108.
37 M. P. Gomes, I. Costa, N. Pébère, J. L. Rossi, B. Tribollet and V. Vivier, *Electrochim. Acta*, 2019, **306**, 61–70.
38 A. D. King, N. Birbilis and J. R. Scully, *Electrochim. Acta*, 2014, **121**, 394–406.
39 Y. Liu, M. Curioni and Z. Liu, *Electrochim. Acta*, 2018, **264**, 101–108.
40 M. Brady, G. Rother, L. Anovitz, K. Littrell, K. Unocic, H. Elsentriecy, G.-L. Song, J. Thomson, N. Gallego and B. Davis, *J. Electrochem. Soc.*, 2015, **162**, C140.
41 J. Čížek, I. Procházka, B. Smola, I. Stulíková, R. Kužel, Z. Matěj, V. Cherkaska, R. Islamgaliev and O. Kulyasova, *Mater. Sci. Eng., A*, 2007, **462**, 121–126.
42 R. Würschum and A. Seeger, *Philos. Mag. A*, 1993, **73**, 1489.
43 B. Oberdorfer and R. Würschum, *Phys. Rev. B: Condens. Matter Mater. Phys.*, 2009, **79**, 184103.
44 R. Würschum, L. Resch and G. Klinser, *Phys. Rev. B*, 2018, **97**, 224108.
45 R. Würschum, L. Resch and G. Klinser, AIP Conf. Proc., 2019, p. 050010.
46 J.-Y. Lee, G. Han, Y.-C. Kim, J.-Y. Byun, J.-i. Jang, H.-K. Seok and S.-J. Yang, *Met. Mater. Int.*, 2009, **15**, 955–961.
47 Y. Wu and Y. Jean, *Phys. Status Solidi A*, 2004, **201**, 917–922.
48 R. Checchetto, N. Bazzanella, A. Kale, A. Miotello, S. Mariazzi, R. Brusa, P. Mengucci, C. Macchi, A. Somoza, W. Egger, *et al.*, *Phys. Rev. B: Condens. Matter Mater. Phys.*, 2011, **84**, 054115.
49 J. Čížek, I. Procházka, F. Bečvář, R. Kužel, M. Cieslar, G. Brauer, W. Anwand, R. Kirchheim and A. Pundt, *Phys. Rev. B: Condens. Matter Mater. Phys.*, 2004, **69**, 224106.
50 K. Sakaki, M. Mizuno, H. Araki and Y. Shirai, *J. Alloys Compd.*, 2006, **414**, 204–206.
51 A. Grill, J. Horky, A. Panigrahi, G. Krexner and M. Zehetbauer, *Int. J. Hydrogen Energy*, 2015, **40**, 17144–17152.
52 G. Song, *Corros. Sci.*, 2007, **49**, 1696–1701.
53 H. Liu, *J. Biomed. Mater. Res., Part A*, 2011, **99**, 249–260.
54 G. Klinser, H. Kren, S. Koller and R. Würschum, *Appl. Phys. Lett.*, 2019, **114**, 013905.
55 F. W. Olver, *NIST Handbook of Mathematical Functions*, Cambridge University Press, 2010.
56 P. Hautojärvi, J. Johansson, A. Vehanen, J. Yli-Kauppila, J. Hillairet and P. Tzanétakis, *Appl. Phys. A*, 1982, **27**, 49–56.
57 J. Čížek, I. Procházka, B. Smola, I. Stulíková, R. Kužel, Z. Matěj, V. Cherkaska, R. K. Islamgaliev and O. B. Kulyasova, *Mater. Sci. Forum*, 2005, 183–186.
58 J. Dryzek, E. Dryzek, T. Suzuki and R. Yu, *Tribol. Lett.*, 2005, **20**, 91–97.
59 R. Nieminen and M. Manninen, *Positrons in solids*, Springer, 1979, pp. 145–195.
60 B. Bergersen, E. Pajanne, P. Kubica, M. Stott and C. Hodges, *Solid State Commun.*, 1974, **15**, 1377–1380.